Quantifying the orbital-to-spin moment ratio under dynamic excitation

Satoru Emori,^{1, a)} Rachel E. Maizel,¹ Galen T. Street,¹ Julia L. Jones,¹ Dario A. Arena,² Padraic Shafer,^{3, b)} and Christoph Klewe³

¹⁾Department of Physics, Virginia Tech, Blacksburg, VA 24060, USA

²⁾ Department of Physics, University of South Florida, Tampa, FL 33620, USA

3) Advanced Light Source, Lawrence Berkeley National Laboratory, Berkeley, CA 94720, USA

(Dated: 24 February 2024)

10

11

12

13

15

16

17

18

19

20

21

22

23

25

26

27

28

31

32

33

34

37

38

40

41

43

The orbital component of magnetization dynamics, e.g., excited by ferromagnetic resonance (FMR), may generate "orbitronic" effects in nanomagnetic devices. Yet, distinguishing orbital dynamics from spin dynamics remains a challenge. Here, we employ x-ray magnetic circular dichroism (XMCD) to quantify the ratio between the orbital and spin components of FMR-induced dynamics in a Ni₈₀Fe₂₀ film. By applying the XMCD sum rules at the Ni $L_{3,2}$ edges, we obtain an orbital-to-spin ratio of 0.108 ± 0.005 for the dynamic magnetization. This value is consistent with 0.102 ± 0.008 for the static magnetization, probed with the same x-ray beam configuration as the dynamic XMCD experiment. The demonstrated method presents a possible path to disentangle orbitronic effects from their spintronic counterparts in magnetic media.

Magnetism generally consists of orbital and spin 51 components. Although orbital magnetism is largely 52 quenched in 3d transition-metal ferromagnets, it can 53 remain up to $\sim 10\%$ of spin magnetism due to spin-54 orbit coupling. 1,2 This seemingly small orbital magnetism 55 yields crucial effects for various device applications, 56 such as magnetic anisotropy for perpendicular magnetic 57 recording and Dzyaloshinkii-Moriya interactions for 58 chiral nanomagnetic memories.^{3–5} The sum-rule analysis ⁵⁹ of x-ray magnetic circular dichroism (XMCD) allows for 60 quantifying the orbital moment μ_L and the spin moment $_{61}$ μ_S in ferromagnets. From XMCD measurements of 62 static magnetization in a transmission geometry, ^{7,8} it is 63 typically straightforward to quantify the ratio μ_L/μ_S of 64 the orbital to spin contributions.

When a ferromagnet is excited, e.g., by ferromagnetic 66 resonance (FMR), its dynamic magnetic response also 67 has orbital and spin components. The value of 68 μ_L/μ_S for the dynamic magnetization may not be 69 equal to that for the static magnetization, as the $_{70}$ orbital and spin dynamics may be distinct. 9,10 For 71 instance, excited orbital angular momentum could be 72 more strongly coupled to the lattice, thereby leading 73 to stronger dissipation. With a greater dynamic loss 74 of orbital moment than spin moment, μ_L/μ_S for the $_{75}$ dynamic magnetization would be smaller than the static 76 counterpart. Indeed, in sub-picosecond demagnetization 77 excited by laser pulses, time-resolved XMCD experiments report a greater reduction of orbital magnetism than spin ${\rm magnetism.}^{9,10}$

Further, recent studies suggest that FMR in a ferromagnet can pump a flow of nonequilibrium orbital angular momentum into an adjacent "sink" layer or interface. ^{11–14} Such FMR-driven orbital pumping is

In this Letter, we quantify μ_L/μ_S of FMR-excited dynamic magnetization in a thin film of permalloy (Ni₈₀Fe₂₀). Our focus here is on the magnetism of Ni, which has greater spin-orbit coupling and hence larger μ_L/μ_S at static equilibrium than Fe.^{2,8} Moreover, the relatively large spin-orbit splitting of the L_3 and L_2 core level manifolds for Ni (the largest among the elemental 3d ferromagnets) facilitates the separation of the XCMD spectral contributions from those core

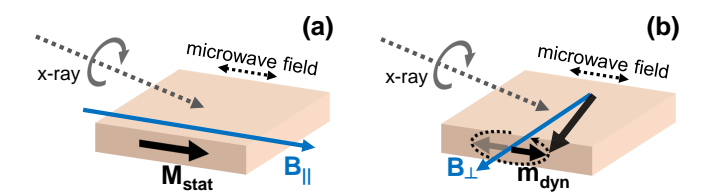


FIG. 1. Schematic illustrations of (a) the static XMCD experiment to probe the static magnetization, $\mathbf{M}_{\mathrm{stat}}$, and (b) the dynamic XMCD experiment to measure the dynamic magnetization, $\mathbf{m}_{\mathrm{dyn}}$.

predicted to coexist with the well-known spin pumping 15 - and may hold the key to understanding the reportedly large "orbitronic" effects in nanomagnetic devices. 16-24 The orbital and spin outflows may be absorbed or scattered differently in the $sink^{25-27}$ or at the ferromagnet interface. 28,29 Again, if the dynamic orbital loss is stronger (or weaker) than the spin loss, μ_L/μ_S for the FMR-excited dynamic magnetization may be reduced (or increased) compared to the static magnetization. We note that conventional FMR spectroscopy is often used to quantify μ_L/μ_S via the well-known g-factor, $(\mu_L/\mu_S)_{\text{FMR}} = (g-2)/2$. However, recent experiments show that $(\mu_L/\mu_S)_{\rm FMR}$ includes an additional spinmixing factor and hence does not generally equal the true value of μ_L/μ_S . Thus, quantifying μ_L/μ_S with XMCD under dynamic excitation is of critical importance for elucidating fundamental angular-momentum dynamics in magnetic materials.

a) Electronic mail: semori@vt.edu

b) Current Affiliation: National Synchrotron Light Source II, Brookhaven National Laboratory, Upton, NY 11973, USA

levels. We have conducted XMCD measurements on both static and dynamic Ni magnetizations in the same sample, probed by the same circularly polarized x-ray beam configuration, as illustrated in Fig. 1. Our work presents a unique way to disentangle FMR-driven orbital dynamics from spin dynamics, which may be of interest for testing orbitronic effects in magnetic multilayers. ^{14,16}

79

80

82

83

86

87

88

89

90

92

93

95

97

98

100

101

102

103

104

105

106

107

108

110

111

112

113

114

115

116

117

118

119

120

121

122

123

124

125

126

127

128

130

131

132

133

134

Our film sample was grown by DC magnetron sputtering at a base pressure of $\approx 3 \times 10^{-8}$ Torr and Ar sputtering gas pressure of 3 mTorr. The film stack structure is MgO(substrate)/Ti(3 nm)/Cu(3 $nm)/Ni_{80}Fe_{20}(30 nm)/Ho(4 nm)/Ti(3 nm).$ MgO substrate (MTI Corp, (001)-oriented) allows for luminescence-yield detection of x-ray absorption.³⁰ Luminescence yield is equivalent to detecting x-ray transmission in the film $sample^7$ and permits more reliable quantification of μ_L/μ_S , compared to total electron yield and fluorescence yield that are prone to $\operatorname{artifacts.}^{31,32}$ All film layers were grown with the substrate at room temperature and were hence polycrystalline. The Ti/Cu seed layer is intended to provide higher-quality growth of ferromagnetic films with narrower FMR linewidths.³³ The overlayer of Ho – a rareearth metal with large orbital magnetism relative to spin magnetism³⁴ – was intended for examining proximityinduced magnetism at the NiFe/Ho interface and its orbital and spin dynamics. However, we were unable to detect Ho magnetism above the noise level of the XMCD measurements. Hereafter, we exclusively focus on XMCD at the Ni $L_{3,2}$ edges.

All measurements were conducted within the same synchrotron beamtime at room temperature at Beamline 4.0.2 of the Advanced Light Source, Lawrence Berkeley National Laboratory. We carried out both static and dynamic XMCD measurements on the same sample holder, equipped with a photodiode for luminescence yield detection and a coplanar waveguide for driving 2-GHz FMR. In this setup, the sample is mounted with the film immediately adjacent to the waveguide. A 90% circularly polarized x-ray beam illuminates the ¹³⁶ sample through a tapered ~ 0.1 -mm-diameter hole in the 137 waveguide's center conductor. The incidence angle of the 138 beam was 40° with respect to the film plane, allowing us¹³⁹ to detect primarily the magnetization component in the film plane. Further details of the experimental setup are found in Ref. 30. We note that a 2-GHz microwave field 141 was applied during both types of measurements [Fig. 1]¹⁴² to ensure a similar temperature. In the static XMCD¹⁴³ experiment, the microwave field was collinear with the equilibrium in-plane magnetization [Fig. 1(a)], so it did 145 not induce FMR. In contrast, the microwave field was orthogonal to the precessional axis to induce FMR in the dynamic XMCD experiment [Fig. 1(b)].

We first demonstrate our static XMCD result₁₅₀ for quantifying μ_L/μ_S of the Ni magnetization at₁₅₁ equilibrium. The x-ray photon energy was stepped discretely from 820 to 909 eV to acquire x-ray absorption₁₅₂ spectra (XAS). At each energy setpoint, the static₁₅₃

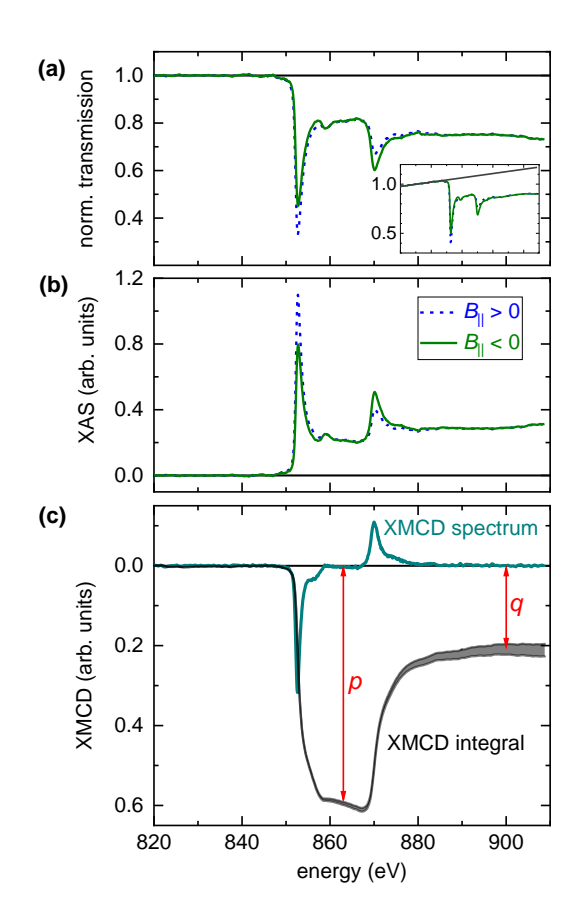


FIG. 2. (a) Normalized x-ray transmission (measured via luminescence yield) and (b) x-ray absorption spectra (XAS) under the opposite directions of the static applied field B_{\parallel} . Inset of (a): Normalized x-ray transmission before subtracting the linear background. (c) Static XMCD spectrum, obtained from the difference between the two XAS spectra in (b), along with the integrated XMCD curve and the parameters p and q used in Eq. 1.

magnetic field, B_{\parallel} , was alternated between +0.3 T and -0.3 T along the incident x-ray beam axis. The circular polarization of the x-ray beam was fixed. To enhance the signal-to-noise ratio, we averaged 23 pairs of XAS scans.

The x-ray transmission intensity was normalized and the linear background [Fig. 2(a) inset] was subtracted to produce the spectra in Fig. 2(a), following the method explained in the Supplementary Material. The normalized transmitted x-ray intensity I is converted to the x-ray absorption $A = -\ln(I)$. Figure 2(b) shows the resulting XAS for $B_{\parallel} = +0.3$ T and -0.3 T. By taking the difference between the XAS at the two opposite magnetization directions, the static XMCD spectrum in Fig. 2(c) was obtained. In producing the XMCD spectrum, we performed post-edge normalization described in the Supplementary Material.

The ratio between the orbital moment μ_L and spin moment μ_S is computed with the standard XMCD sum-

4 rule formula,

155

156

157

158

159

160

161

162

163

164

165

167

168

169

170

171

172

173

174

175

176

177

178

179

180

181

182

183

$$\frac{\mu_L}{\mu_S^{\text{eff}}} \approx \frac{\mu_L}{\mu_S} = \frac{2}{3} \left(\frac{q}{3p - 2q} \right),\tag{1}$$

where q is the value of the integrated XMCD spectrum across the L_3 and L_2 edges, whereas p is the value of the integrated XMCD spectrum across only the L_3 edge.⁶ Figure 2(c) shows the integrated XMCD spectrum and the definitions of q and p. Here, q is obtained in the post-edge energy range (explained in the Supplementary Material), and p is obtained using the cutoff energy of 863 eV that delineates the L_3 and L_2 core level manifolds. Strictly speaking, the denominator in Eq. 1 is the "effective" spin moment $\mu_S^{\text{eff}} = \mu_S - 7 \langle T_z \rangle \mu_B / \hbar$ that includes the expectation value of the magnetic dipole operator $\langle T_z \rangle$. The $7 \langle T_z \rangle$ term can exceed a few percent of μ_S in atomically-thin 3d ferromagnets, but it diminishes to an undetectable level when the 3dferromagnet thickness is several atomic monolayers or greater^{8,35,36}. In our present 30-nm-thick permalloy film, we safely assume that $\mu_S^{\text{eff}} = \mu_S$.

From the static XMCD experiment, we arrive at an orbital-to-spin ratio of $\mu_L/\mu_S \approx 0.102$ by applying Eq. 1. This value is comparable to the typical μ_L/μ_S of ~ 0.1 for Ni in permalloy in recent XMCD experiments.^{8,37} We identify an uncertainty of ± 0.008 for μ_L/μ_S due to the variation in the outcome of the post-edge normalization¹⁸⁵ (see Supplementary Material). This uncertainty is ¹⁸⁶ graphically represented as a shaded band in Fig. 2(c). ¹⁸⁷

We now describe our time-resolved dynamic XMCD¹⁸⁸ experiment, with the sample magnetized by the external¹⁸⁹ field B_{\perp} orthogonal to the x-ray beam [Fig. 1(b)].¹⁹⁰ The magnetization was excited by a 2-GHz microwave¹⁹¹ field and precesses about B_{\perp} . The circularly polarized¹⁹²

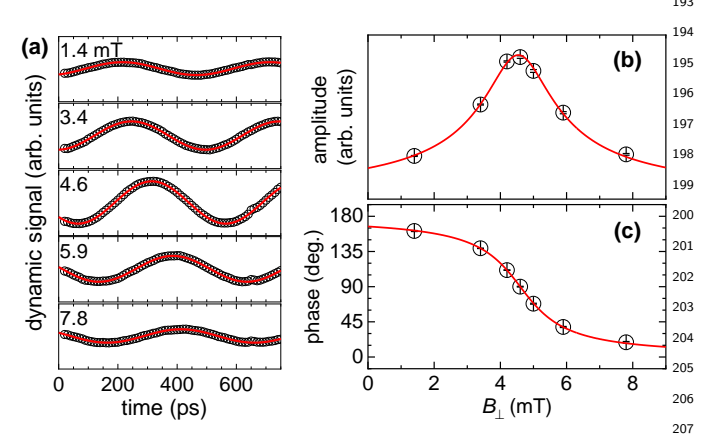


FIG. 3. (a) Time traces of the differential dynamic x-ray transmission signal, arising from FMR-induced magnetization oscillations, at several values of applied field B_{\perp} (orthogonal to the x-ray beam axis, see Fig. 1(a)). The photon energy is 1 fixed at the peak of the Ni L_3 edge. (b,c) B_{\perp} dependence of 12 the precessional (b) amplitude and (c) phase. The symbols 213 are the values derived from the measurements. The red curves 214 represent the best fits, from which the resonance field $B_{\rm res} \approx 215$ 4.5 mT is quantified.

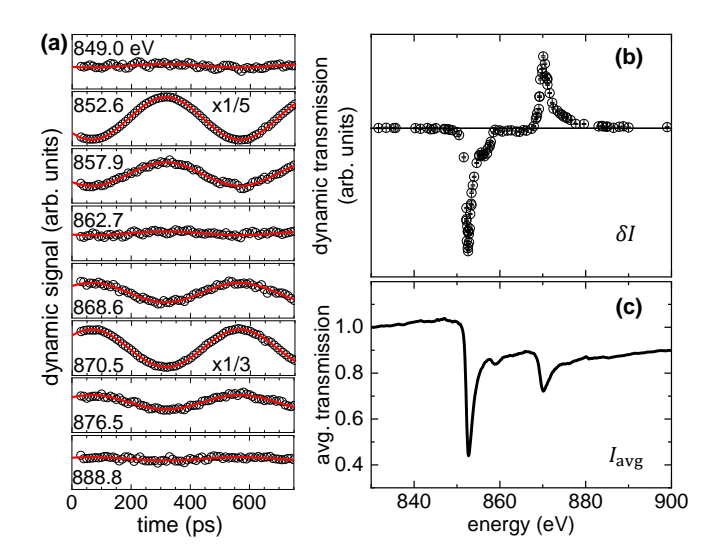


FIG. 4. (a) Time traces of the differential dynamic x-ray transmission signal, arising from FMR-induced magnetization oscillations, at several values of photon energy. The field B_{\perp} is fixed at $B_{\rm res}=4.5$ mT. (b,c) Energy dependence of (b) the amplitude of the differential x-ray transmission, δI , and (c) the equilibrium average x-ray transmission, $I_{\rm avg}$, derived from the average of the two curves in the inset of Fig. 2(a).

x-ray beam probed the FMR-induced dynamics of the nonequilibrium magnetization ($\mathbf{m}_{\rm dyn}$ in Fig. 1(b)). Similar to the normalization of the static transmission signal (described in the Supplementary Material), the dynamic transmission signal acquired via lockin detection³⁰ was normalized by the incident beam intensity upstream at the end station detector of the beamline.

Figure 3(a) shows time traces of the dynamic differential x-ray transmission signal obtained at a fixed photon energy of 852.8 eV and different B_{\perp} , employing the phase-modulated lock-in protocol outlined in Refs. 30 and 38. These traces are fit excellently by sinusoids with an oscillation period of 500 ps, as expected from the 2-GHz microwave excitation. From each fit, we extract both the amplitude and phase of the dynamic magnetization. Figures 3(b) and (c) reveal a peak in the amplitude and a 180° shift in the phase, which are consistent with FMR. ^{39–41} The resonance field $B_{\rm res} \approx 4.5$ mT is obtained by fitting the B_{\perp} dependence of the amplitude with $\propto \sqrt{\Delta B^2/(\Delta B^2 + (B_{\perp} - B_{\rm res})^2)}$ and that of the phase with $\phi_o + \operatorname{atan}(\Delta B/(B_{\perp} - B_{\rm res}))$. The fits also yield the FMR linewidth, $\Delta B \approx 1.0$ mT; the phase offset ϕ_o from the experimental setup is shifted to 0 in Fig. 3(c) for clarity.

To quantify μ_L/μ_S for the dynamic magnetization, it is necessary to measure the energy dependence of the dynamic XMCD signal. All following measurements were performed at $B_{\perp}=B_{\rm res}$ to maximize the signal amplitude. As shown in Fig. 4(a), time traces of differential x-ray transmission reveal sinusoidal oscillations. All have the same period of 500 ps, but

the phase exhibits a discrete 180° shift, corresponding to₂₆₉ the sign of the static XMCD signal at that energy (e.g.,₂₇₀ compare 852.6 eV near the L_3 edge maximum amplitude₂₇₁ with 870.5 eV near the L_2 edge maximum). By plotting₂₇₂ the energy dependence of the oscillation amplitude₂₇₃ [Fig. 4(b)], we observe a trend that resembles the XMCD₂₇₄ spectrum for the static magnetization [Fig. 2(c)].

218

219

221

222

224

225

227

228

231

232

233

237

238

239

240

241

244

245

247

249

250

252

253

254

255

256

257

258

259

261

262

264

265

267

Yet, caution must be taken before applying the XMCD₂₇₆ sum rules. What is shown in Fig. 4(b) is the amplitude of 277 the measured differential x-ray transmission, $\delta I = I^-$ – 278 I^+ , between the dynamic magnetization oriented parallel 279 (I^+) and antiparallel (I^-) to the incident beam. To₂₈₀ analyze dynamic XMCD properly, δI must be converted 281 to the differential x-ray absorption,

$$\delta A = \ln(I^+) - \ln(I^-).$$
 (2)₂₈₄

Since the precessional cone angle here is only $\sim 1^{\circ}$, δI_{286}^{-} is a small perturbation about the average transmission₂₈₇ $I_{\rm avg}$, such that $I^{\pm} = I_{\rm avg} \pm \delta I/2$ with $\delta I \ll I_{\rm avg}$. Then₂₈₈ we can re-write Eq. 2 as

$$\delta A = \ln\left(1 + \frac{\delta I}{2I_{\text{avg}}}\right) - \ln\left(1 - \frac{\delta I}{2I_{\text{avg}}}\right) \approx \frac{\delta I}{I_{\text{avg}}}. \quad (3)_{\frac{291}{292}}^{290}.$$

We take $I_{\rm avg}$ from Fig. 4(c), which is the average of the static transmission spectra at $B_{\parallel} > 0$ and < 0 [inset of Fig. 2(a)]. The resulting dynamic XMCD amplitude δA obtained from Eq. 3 is presented in Fig. 5(a). This analysis protocol is crucial for deriving an accurate dynamic XMCD spectrum; applying the XMCD sum rules on δI vs energy [Fig. 4(b)] would result in an incorrect estimation of μ_L/μ_S . We also remark that, in principle, $I_{\rm avg}$ can be obtained from the DC luminescence yield signal acquired simultaneously with the dynamic signal. However, in practice, our detection electronics (optimized for the dynamic luminescence yield signal) did not produce a sufficient signal-to-noise ratio for the DC signal, such that $I_{\rm avg}$ needed to be obtained from a separate set of static measurements [Fig. 2].

Figure 5 is the central result of this study. Figure 5(a) reveals that the dynamic XMCD data closely track the static XMCD spectrum. This close correspondence already suggests that μ_L/μ_S is similar for the dynamic magnetization and the static magnetization. Further, comparing the XMCD integrals for the dynamic and static cases in Fig. 5(b) again reveals close agreement.

Nevertheless, by applying the sum-rule analysis (Eq. 1) to the dynamic XMCD integral, we obtain $(\mu_L/\mu_S)_{\rm dyn} \approx 0.108$. This value is noticeably higher than the mean $(\mu_L/\mu_S)_{\rm stat} \approx 0.102$ for the static magnetization. The possibility that $(\mu_L/\mu_S)_{\rm dyn} > (\mu_L/\mu_S)_{\rm stat}$ would suggest stronger dissipation for spin dynamics than orbital dynamics. This is contrary to the intuitive expectation of stronger orbital dissipation by the more direct orbital-to-lattice coupling. A potential explanation is that the thin Ho layer, interfaced with the permalloy film, more efficiently absorbs FMR-pumped nonequilibrium spin angular momentum than orbital angular momentum.

However, from our present XMCD results alone, we are unable to conclude that dynamic spin dissipation is stronger than orbital dissipation – or that $(\mu_L/\mu_S)_{\rm dyn}$ is higher than $(\mu_L/\mu_S)_{\rm stat}$. Considering the uncertainty in q due to the limited post-edge data density for the dynamic XMCD, the uncertainty in $(\mu_L/\mu_S)_{\rm dyn}$ may Accounting for the uncertainties be up to ± 0.005 . in our static and dynamic XMCD results, we have $(\mu_L/\mu_S)_{\rm dyn} = 0.108 \pm 0.005$ and $(\mu_L/\mu_S)_{\rm stat} = 0.102 \pm$ 0.008 – i.e., the values of $(\mu_L/\mu_S)_{\rm dyn}$ and $(\mu_L/\mu_S)_{\rm stat}$ are indistinguishable. Moreover, there are conceivably additional sources of uncertainty for $(\mu_L/\mu_S)_{\rm stat}$, as the setup here was optimized for dynamic XMCD but not for static XMCD. For instance, the substrate may have an energy-dependent luminescence vield background⁷ that distorts the XAS spectrum, although it is yet unclear how this may affect the XMCD spectrum; the influence of such a substrate-dependent background may be investigated in future experiments. the extended averaging, our derived $(\mu_L/\mu_S)_{\rm stat}$ may also be affected by small fluctuations of the static XMCD measurements. Considering the points above, $(\mu_L/\mu_S)_{\rm stat}$ and $(\mu_L/\mu_S)_{\rm dyn}$ are essentially identical within experimental uncertainty for this particular

In summary, we have employed XMCD to quantify the orbital-to-spin ratio μ_L/μ_S of FMR-excited dynamic magnetization in a permalloy film. This dynamic μ_L/μ_S ratio turns out to agree closely with its static counterpart to within a few %. Our present results cannot determine conclusively whether FMR-driven orbital dynamics

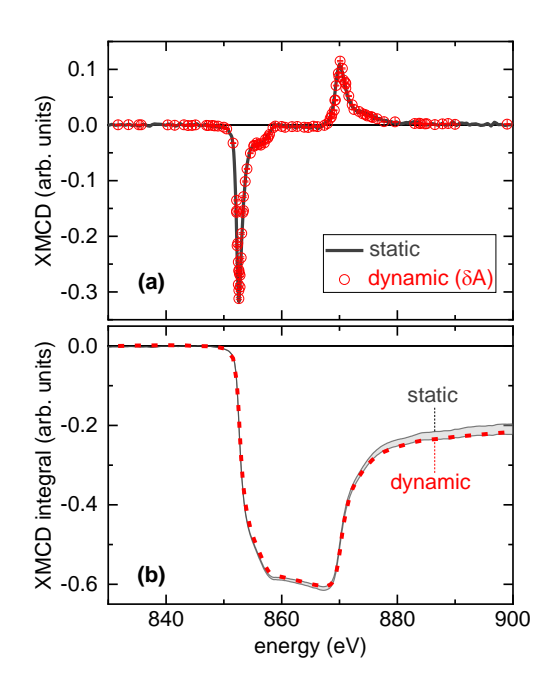


FIG. 5. Energy dependence of (a) the static and dynamic XMCD amplitudes and (b) the XMCD integrals. The dynamic XMCD data (δA) are derived by applying Eq. 3 to the data shown in Fig. 4(b,c).

differs from spin dynamics. Nevertheless, in future353 studies, experimental uncertainties may be tightened354 for a more precise quantification of μ_L/μ_S . Future... work will also benefit from studying a series of samples₃₅₇ with different compositions and layer structures. systematic relative variation in the dynamic μ_L/μ_S ratio³⁵⁹ among these samples may uncover orbital dissipation³⁶⁰ that is distinct from its spin counterpart. ^{26–29} Moreover, ³⁶¹ the dynamic XMCD method may allow for resolving 363 the variation of μ_L/μ_S during magnetic precession⁴² in₃₆₄ a highly anisotropic, single-crystalline magnetic film, 365 whose orbital magnetism is strongly linked to the crystal³⁶⁶ orientation. Such time-resolved mapping of μ_L/μ_S may 367 provide direct insights into the breathing Fermi surface $_{369}^{--}$ mechanism that governs intrinsic magnetic damping. 43,44₃₇₀ Overall, our unique approach provides an avenue for³⁷¹ quantitatively evaluating dynamic orbital-based effects³⁷² - beyond the conventional spin-based picture - in_{374}^{373} nanomagnetic structures.

See the Supplementary Material for additional³⁷⁷ information on the post-edge normalization of the³⁷⁸ static XMCD spectrum.

381

382

383

405

406

407

ACKNOWLEDGEMENTS

301

302

304

305

307

308

310

311

313

314

316

317

318

319

320

321

322

324

326

328

329

331

332

334

335

337

338

340

341

342

343

349

350

351

352

S.E. and G.T.S. were supported by the Air Force₃₈₆ Office of Scientific Research under Grant No. FA9550-387 R.E.M. and J.L.J. were supported by³⁸⁸ the National Science Foundation under ENG-ECCS-389 D.A.A. acknowledges support from the 391 2144333. National Science Foundation under grant ENG-ECCS-392 1952957. P.S. and C.K. acknowledge partial support³⁹³ from the U.S. Department of Energy, Office of Science, 394 Office of Basic Energy Sciences, Materials Sciences and 395 Engineering Division under Contract No. DE-AC02-05-397 CH11231 (Codesign of Ultra-Low-Voltage Beyond CMOS₃₉₈ Microelectronics for the development of materials for low-399 power microelectronics). The Advanced Light Source is 400 supported by the Director, Office of Science, Office of d_{402}^{401} Basic Energy Sciences, of the U.S. Department of Energy₄₀₃ under Contract No. DE-AC02-05CH11231.

DATA AVAILABILITY

The data that support the findings of this study are⁴¹⁰ available from the corresponding author upon reasonable⁴¹¹ request.

- ¹R. C. O'Handley, Modern Magnetic Materials: Principles and ⁴¹⁵
 Applications (Wiley-Interscience, 1999).
- ²M. A. W. Schoen, J. Lucassen, H. T. Nembach, T. J. Silva, 417
 B. Koopmans, C. H. Back, and J. M. Shaw, Physical Review 418
 B 95, 134410 (2017).
 - ³B. Dieny and M. Chshiev, Reviews of Modern Physics **89**, 025008₄₂₀ (2017).
 - ⁴J. Okabayashi, J. W. Koo, H. Sukegawa, S. Mitani, Y. Takagi, and T. Yokoyama, Applied Physics Letters 105, 122408 (2014).

- ⁵S. Kim, K. Ueda, G. Go, P.-H. Jang, K.-J. Lee, A. Belabbes, A. Manchon, M. Suzuki, Y. Kotani, T. Nakamura, K. Nakamura, T. Koyama, D. Chiba, K. T. Yamada, D.-H. Kim, T. Moriyama, K.-J. Kim, and T. Ono, Nature Communications 9, 1648 (2018).
- ⁶C. T. Chen, Y. U. Idzerda, H. J. Lin, N. V. Smith, G. Meigs, E. Chaban, G. H. Ho, E. Pellegrin, and F. Sette, Physical Review Letters 75, 152 (1995).
- ⁷C. Piamonteze, Y. W. Windsor, S. R. Avula, E. Kirkc, and U. Staub, Journal of Synchrotron Radiation 27, 1289 (2020).
- ⁸J. M. Shaw, R. Knut, A. Armstrong, S. Bhandary, Y. Kvashnin, D. Thonig, E. K. Delczeg-Czirjak, O. Karis, T. J. Silva, E. Weschke, H. T. Nembach, O. Eriksson, and D. A. Arena, Physical Review Letters 127, 207201 (2021).
- ⁹C. Boeglin, E. Beaurepaire, V. Halté, V. López-Flores, C. Stamm, N. Pontius, H. A. Dürr, and J. Y. Bigot, Nature 2010 465:7297 465, 458 (2010).
- ¹⁰N. Bergeard, V. López-Flores, V. Halté, M. Hehn, C. Stamm, N. Pontius, E. Beaurepaire, and C. Boeglin, Nature Communications 2014 5:1 5, 1 (2014).
- ¹¹E. Santos, J. Abrão, D. Go, L. de Assis, Y. Mokrousov, J. Mendes, and A. Azevedo, Physical Review Applied 19, 014069 (2023).
- ¹²A. E. Hamdi, J. Y. Chauleau, M. Boselli, C. Thibault, C. Gorini, A. Smogunov, C. Barreteau, S. Gariglio, J. M. Triscone, and M. Viret, Nature Physics 2023, 1 (2023).
- $^{13}{\rm H.}$ Hayashi, D. Go, Y. Mokrousov, and K. Ando, arXiv , 2304.05266~(2023).
- ¹⁴D. Go, K. Ando, A. Pezo, S. Blügel, A. Manchon, and Y. Mokrousov, arXiv, 2309.14817 (2023).
- ¹⁵Y. Tserkovnyak, A. Brataas, G. E. W. Bauer, and B. I. Halperin, Reviews of Modern Physics 77, 1375 (2005).
- ¹⁶D. Go, D. Jo, H. W. Lee, M. Kläui, and Y. Mokrousov, Europhysics Letters 135, 37001 (2021).
- ¹⁷S. Ding, A. Ross, D. Go, L. Baldrati, Z. Ren, F. Freimuth, S. Becker, F. Kammerbauer, J. Yang, G. Jakob, Y. Mokrousov, and M. Kläui, Physical Review Letters 125, 177201 (2020).
- ¹⁸D. Lee, D. Go, H. J. Park, W. Jeong, H. W. Ko, D. Yun, D. Jo, S. Lee, G. Go, J. H. Oh, K. J. Kim, B. G. Park, B. C. Min, H. C. Koo, H. W. Lee, O. J. Lee, and K. J. Lee, Nature Communications 2021 12:1 12, 1 (2021).
- ¹⁹C. Y. Hu, Y. F. Chiu, C. C. Tsai, C. C. Huang, K. H. Chen, C. W. Peng, C. M. Lee, M. Y. Song, Y. L. Huang, S. J. Lin, and C. F. Pai, ACS Applied Electronic Materials 4, 1099 (2022).
- ²⁰A. Rothschild, N. Am-Shalom, N. Bernstein, M. Meron, T. David, B. Assouline, E. Frohlich, J. Xiao, B. Yan, and A. Capua, Physical Review B 106, 144415 (2022).
- ²¹H. Hayashi, D. Jo, D. Go, T. Gao, S. Haku, Y. Mokrousov, H.-W. Lee, and K. Ando, Communications Physics 2023 6:1 6, 32 (2023).
- ²²Y. G. Choi, D. Jo, K. H. Ko, D. Go, K. H. Kim, H. G. Park, C. Kim, B. C. Min, G. M. Choi, and H. W. Lee, Nature 2023 619:7968 **619**, 52 (2023).
- ²³I. Lyalin, S. Alikhah, M. Berritta, P. M. Oppeneer, and R. K. Kawakami, Physical Review Letters 131, 156702 (2023).
- ²⁴G. Sala, H. Wang, W. Legrand, and P. Gambardella, Physical Review Letters 131, 156703 (2023).
- ²⁵G. Sala and P. Gambardella, Physical Review Research 4, 033037 (2022).
- ²⁶D. Go, D. Jo, K. W. Kim, S. Lee, M. G. Kang, B. G. Park, S. Blügel, H. W. Lee, and Y. Mokrousov, Physical Review Letters 130, 246701 (2023).
- ²⁷A. Manchon, A. Pezo, K.-W. Kim, and K.-J. Lee, arXiv, 2310.04763 (2023).
- ²⁸K. D. Belashchenko, G. G. B. Flores, W. Fang, A. A. Kovalev, M. van Schilfgaarde, P. M. Haney, and M. D. Stiles, Physical Review B **108**, 144433 (2023).
- $^{29}\mathrm{S}.$ Urazhdin, Physical Review B $\mathbf{108},$ L180404 (2023).
- ³⁰C. Klewe, Q. Li, M. Yang, A. T. N'Diaye, D. M. Burn, T. Hesjedal, A. I. Figueroa, C. Hwang, J. Li, R. J. Hicken, P. Shafer, E. Arenholz, G. van der Laan, and Z. Qiu, Synchrotron

Radiation News **33**, 12 (2020).

423

424

425

429

430

³¹R. Nakajima, J. Stöhr, and Y. U. Idzerda, Physical Review B₄₄₄
 59, 6421 (1999).

32 B. Liu, C. Piamonteze, M. U. Delgado-Jaime, R. P. Wang, 446
 J. Heidler, J. Dreiser, R. Chopdekar, F. Nolting, and F. M. D. 447
 Groot, Physical Review B 96, 054446 (2017).

33 E. R. Edwards, H. T. Nembach, and J. M. Shaw, Physical 449
 Review Applied 11, 054036 (2019).

431 34S. G. Reidy, L. Cheng, and W. E. Bailey, Applied Physics Letters
 452 82, 1254 (2003).

35 M. Gottwald, S. Andrieu, F. Gimbert, E. Shipton, L. Calmels, 453
 C. Magen, E. Snoeck, M. Liberati, T. Hauet, E. Arenholz, 454
 S. Mangin, and E. E. Fullerton, Physical Review B - Condensed 455
 Matter and Materials Physics 86, 014425 (2012).

Andrieu, T. Hauet, M. Gottwald, A. Rajanikanth, L. Calmels, 457
 A. M. Bataille, F. Montaigne, S. Mangin, E. Otero, P. Ohresser, 458
 P. L. Fèvre, F. Bertran, A. Resta, A. Vlad, A. Coati, and 459
 Y. Garreau, Physical Review Materials 2, 064410 (2018).

⁴⁴¹ ³⁷B. Glaubitz, S. Buschhorn, F. Brüssing, R. Abrudan, and ⁴⁶¹
 ⁴⁴² H. Zabel, Journal of Physics: Condensed Matter 23, 254210462

(2011).

443

³⁸D. A. Arena, E. Vescovo, C.-C. Kao, Y. Guan, and W. E. Bailey, Physical Review B **74**, 064409 (2006).

³⁹Y. Guan, W. Bailey, E. Vescovo, C.-C. Kao, and D. Arena, Journal of Magnetism and Magnetic Materials 312, 374 (2007).

⁴⁰ J. Li, L. R. Shelford, P. Shafer, A. Tan, J. X. Deng, P. S. Keatley, C. Hwang, E. Arenholz, G. van der Laan, R. J. Hicken, and Z. Q. Qiu, Physical Review Letters 117, 076602 (2016).

⁴¹A. A. Baker, A. I. Figueroa, C. J. Love, S. A. Cavill, T. Hesjedal, and G. van der Laan, Physical Review Letters 116, 047201 (2016).

⁴²D. A. Arena, Y. Ding, E. Vescovo, S. Zohar, Y. Guan, and W. E. Bailey, Review of Scientific Instruments 80, 83903 (2009).

⁴³K. Gilmore, Y. U. Idzerda, and M. D. Stiles, Physical Review Letters 99, 027204 (2007).

⁴⁴B. Khodadadi, A. Rai, A. Sapkota, A. Srivastava, B. Nepal, Y. Lim, D. A. Smith, C. Mewes, S. Budhathoki, A. J. Hauser, M. Gao, J.-F. Li, D. D. Viehland, Z. Jiang, J. J. Heremans, P. V. Balachandran, T. Mewes, and S. Emori, Physical Review Letters 124, 157201 (2020).